ADVANCED ELECTRONIC MATERIALS
Open Access
www.advelectronicmat.de

Organic Photo-Responsive Piezoelectric Materials Based on Pyrene Molecules for Flexible Sensors

Xinyi Song, Xiaohui Wang, Wei Liu, Xiaoxue Chen, Shaoling Li, Md Shariful Islam, Ling Li, Xiaobo Zhao, Carl Redshaw, Yu Zhao, Changyong (Chase) Cao,* and Xing Feng**

Due to the advantages of multiplicity, functionality, and flexibility of organic building blocks, organic piezoelectric materials are regarded as next-generation materials for potential applications in flexible sensors and energy harvesting devices. Here, a new pure organic pyrene-based molecule, PyPT is presented, which crystallizes in a non-centrosymmetric structure. PyPT is synthesized and demonstrated to be suitable for developing flexible sensors due to its remarkable piezoelectric properties. The pyrene-based piezoelectric molecule exhibits excitation wavelength-dependent emission behavior and aggregation-caused quenching properties and demonstrated a piezoelectric coefficient (d_{33}) of 8.02 ± 0.26 pm V^{-1}. The output electronic signal of a PyPT-based flexible sensor shows a significant increase from 30 to 721 pA as the strain increases from 0.12% to 0.59% with a low Young's modulus of 1.63 Gpa. This high-performance piezoelectric sensor can serve as a sensitive sound sensor for sound detection and recognition based on the basic characteristics of sound, such as amplitude, frequencies, and timbres. This research offers new insights into advancing pure organic luminescent materials with piezoelectric properties, paving the way for applications in flexible electronics for wearables, human–machine interfaces, and the Internet of Things.

1. Introduction

The piezoelectric effect is an inherent property of noncentrosymmetric crystals where electrical and mechanical energy are mutually convertible.[1,2] Theoretically, the essence of the piezoelectric effect is the electrical polarization against external strains in noncentral symmetric lattices. The development of novel materials with piezoelectric properties has attracted increasing attention in the emerging field of materials science, flexible devices,[3] and energy storage.[4,5] Since the piezoelectric effect was first observed in quartz crystals,[6] a variety of piezoelectric materials have been explored for advanced applications in wearable devices, energy harvesters,[7] igniters,[8] and many others. These materials include inorganic piezoelectric materials (e.g., lead zirconate titanate (PZT),[9] barium titanate ($BaTiO_3$, BTO),[10] Zinc Oxide (ZnO),[11] polymer piezoelectric materials (e.g., polyvinylidene fluoride (PVDF)[12,13]), and natural piezoelectric biomaterials (e.g., wood, bone).[14]

Among these materials, PZT is widely used in high-performance piezoelectric devices and sensors due to its high piezoelectric coefficient and good piezoelectric coupling coefficient.[15,16] However, PZT is prone to polarization degradation during long-term use, leading to a decrease in piezoelectric performance. Additionally, the toxic lead in PZT can cause environmental pollution if improperly disposed of.[17,18] On the other hand, organic piezoelectric materials offer several advantages, such as lower Young's modulus, environmental friendliness, and functionalizability, making them suitable for developing flexible piezoelectric devices.[19]

While bio-organic and natural biomaterials with piezoelectric effects have high biocompatibility and show promise in metabolic systems and biomedical engineering,[20] they often suffer from weak piezoelectric signals and limited scalability. Given

---

X. Song, X. Wang, W. Liu, X. Chen, S. Li, X. Zhao, Y. Zhao, X. Feng
Guangdong Provincial Key Laboratory of Functional Soft Condensed Matter, School of Material and Energy
Guangdong University of Technology
Guangzhou 510006, China
E-mail: hyxhn@sina.com

The ORCID identification number(s) for the author(s) of this article can be found under https://doi.org/10.1002/aelm.202400933

DOI: 10.1002/aelm.202400933

M. S. Islam, C. (Chase) Cao
Department of Mechanical and Aerospace Engineering
Case Western Reserve University
Cleveland, OH 44106, USA
E-mail: ccao@case.edu

L. Li
School of Semiconductor Science and Technology
South China Normal University
Foshan 528225, China
E-mail: linglids@sina.com

C. Redshaw
Chemistry
School of Natural Sciences
University of Hull
Hull, Yorkshire HU6 7RX, UK

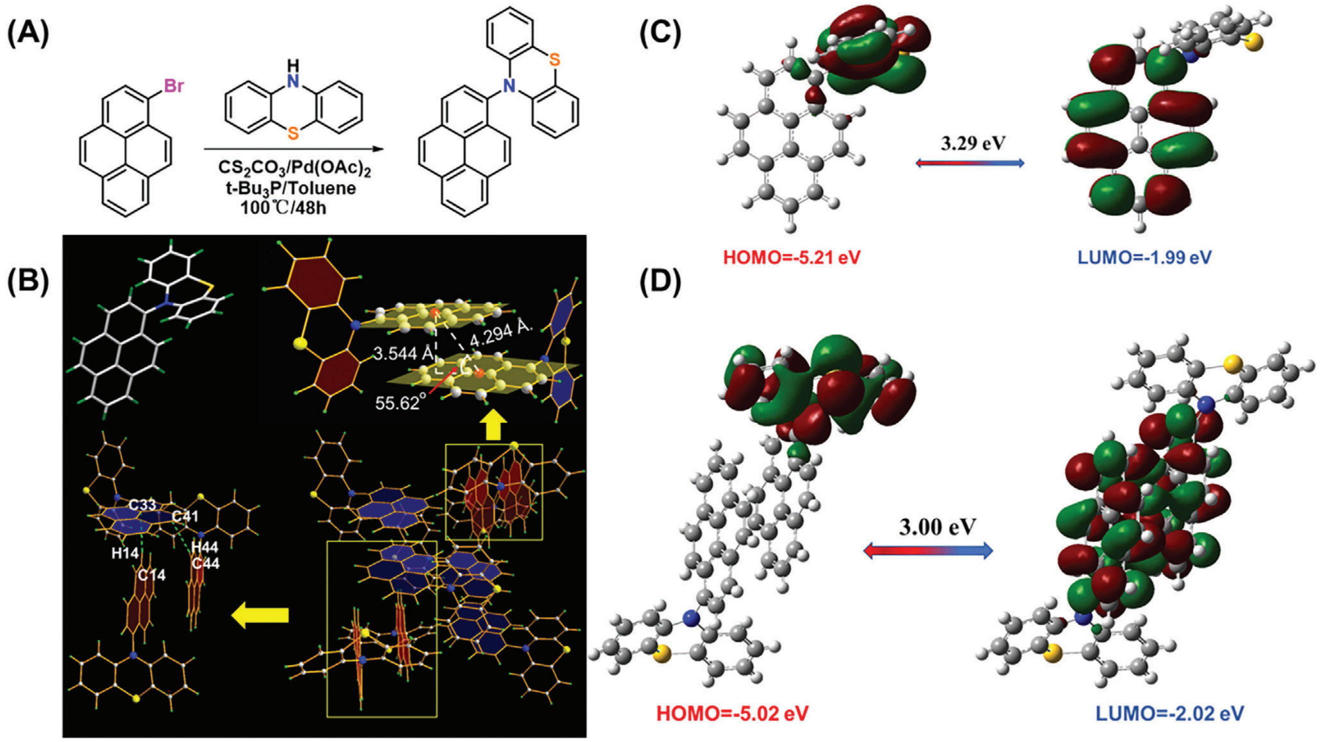

Figure 1. Synthesis and schematic illustration of PyPT. A) Synthesis of compound PyPT. B) Crystal structure of PyPT and packing structure via π–π stacking. C) Optimized molecular orbital diagrams of a single molecule of PyPT, calculated at B3LYP/6-311G(d,p) level of theory. D) Optimized molecular orbital diagrams of a dimer of PyPT, calculated at B3LYP/6-311G(d,p) level of theory.

the advantages of functionalizing and flexible organic building blocks, significant efforts have been devoted to developing new organic polymers or organic–inorganic hybrid piezoelectric materials through molecular engineering to meet various scientific and industrial needs.[21,22] For instance, Xiong and coworkers reported a single-phase organic-inorganic perovskite piezoelectric molecule (trimethylchloromethyl ammonium trichloromanganese (II) ($TMCM\text{-}MnCl_3$) with a large piezoelectric coefficient (d_{33}) of 185 pC N^{-1}, comparable to traditional piezoelectric ceramic barium titanate (BTO).[23] Additionally, trimethylfluoromethyl ammonium functionalized perovskite ($TMFM\text{-}CdCl_3$) exhibits an even higher d_{33} of 1540 pC N^{-1}.[24] The typical organic polymer (PVDF) can act as a flexible piezoelectric material for wearable and medical devices, but only the β-phase-rich PVDF possesses d_{33} (13-28 pC N^{-1}) and low dielectric constants ε ($\approx$30).[25,26] Thus, researchers often explore PVDF-based piezoelectric materials via doping strategies.[27]

In contrast, pure organic molecules exhibit flexible molecular skeletons, and tunable molecular and electronic structures via molecular engineering, and their electrical polarization is sensitive to the external environment, such as solvent polarity, temperature, and mechanical forces. Pyrene,[28,29] composed of four phenyl-fused polycyclic aromatic hydrocarbon rings in a rhombic structure, emits bright blue emission in solution (λ_{em} = 372 nm, $\Phi_f = 0.64$)[30] and exhibits a sensitive microenvironment-independent emission change.[28] Thus, pyrene can act as an electron donor or acceptor depending on the peripheral substituents and prefers to form a π-stacking pattern through weak intra- and intermolecular interactions.[31,32]

Inspired by the classical piezoelectric mechanism, the unique electronic effect of pyrene, and the diverse molecular conformations of the phenothiazine unit,[33,34] we have designed a pure organic pyrene-based molecule, **PyPT**, containing a phenothiazine unit. This new molecule not only exhibits fantastic emission behavior in solution but also shows an excellent anisotropic-dependent piezoelectric effect in its non-centrosymmetric crystal form under external strain. The maximum electrical output is up to 721 pA under a strain of 0.59% along the (010) axis, with a d_{33} value of 8.02 ± 0.26 pm V^{-1}. Additionally, the pyrene-based single-crystal piezoelectric sensor was demonstrated to sensitively detect sound via an acoustic-electric conversion process, and capable of identifying basic sound characteristics (such as amplitude, frequencies, and timbres). Different sounds from musical instruments can also output differentiated electric signals, enabling the analysis of acoustic sources by combining data science and machine learning for broad applications.

2. Results and Discussion

2.1. Synthesis and Characterization of PyPT

The synthetic route to the pyrene-based molecule **PyPT** is presented in **Figure** 1A. A Buchwald–Hartwig coupling reaction of 1-bromopyrene and phenothiazine afforded the pyrene-based compound **PyPT** in 37% yield. The compound was fully characterized by $^{1}H/^{13}C$ NMR spectroscopy (Figures S1,S2, Supporting information), high-resolution mass spectrometry (Figure S3, Supporting information) and single-crystal X-ray diffraction analysis. The single crystal of **PyPT** was cultivated from a mixed n-hexane and dichloromethane solution via the solvent evaporation method. The basic crystallographic information is summarized in Table S1 (Supporting information).

PyPT crystallized in the monoclinic system with the non-centrosymmetric space group of Pna21, and the unit cell contains eight molecules. As shown in Figure 1B, there is a highly distorted conformation between the phenothiazine and pyrene rings, with an almost perpendicular dihedral angle (more than 85°). Two phenyl rings in the phenothiazine unit are not coplanar, forming a dihedral angle of 22.20°. This molecular conformation has subtle differences compared to those previously reported.[35]

The molecule is arranged as a pair of dimers via head-to-tail, and face-to-face π–π stacking at 3.544 Å. Generally, an H-aggregate is defined as the molecule arranged in a face-to-face π–π stacking with an aligned angle larger than 54.7°. In this case, the centroid–-centroid distance between the two pyrenes is 4.294 Å, resulting in an aligned angle of 55.62°. According to the McRaés theory,[36] this type of crystal packing belongs to the H-aggregate form (Figure 1B), which contributes to facilitating charge transport and increasing charge carrier mobility.[37,38] The phenothiazines are connected to the adjacent pyrene ring via C-H···π interactions (C14-H14···C33: 2.988 Å, C44-H44···C41: 3.100 Å). Two dimers are vertical to each other via a C-H···π interaction (Figure 1B). These pairs of dimers may endow the system with new photophysical properties.

Furthermore, the ground state geometric conformation of **PyPT** was optimized at the B3LYP/6-311G (d,p) level using density functional theory (DFT) calculations to understand the effect of the electronic structure distribution on the molecular optical properties. The highest occupied molecular orbital (HOMO) and lowest unoccupied molecular orbital (LUMO) energy levels are shown in Figure 1C. Due to the strong electron-donating ability of phenothiazines, the HOMO of **PyPT** is mainly distributed over the phenothiazines unit, while the LUMO is distributed over the pyrene ring with weak electron-withdrawing groups. The almost complete separation of the HOMO and LUMO further confirms the intramolecular charge transfer (ICT) effect of **PyPT**, consistent with the emission spectra. Furthermore, the pyrene-based dimer structures were optimized according to the single crystal. As shown in Figure 1D, the HOMO, and LUMO are mainly concentrated on the phenothiazines units and the entire pyrene ring, respectively. The energy gap decreased from 3.29 eV for the monomer to 3.00 eV for the dimer, indicating a change in electronic properties due to dimerization.

2.2. Photophysical Properties of PyPT

The UV–vis absorption and photoluminescence (PL) spectra of **PyPT** were measured in THF solution (10^{-5} M) and in the solid state at room temperature. As shown in **Figure 2A**, **PyPT** displays "pyrene-like" absorption with a red-shifted absorption band at 341 nm (molar absorption coefficient ε: 11600 M^{-1} cm^{-1}) compared to the unsubstituted pyrene ($\lambda_{\text{max abs}}$ = 335 nm). Upon excitation, **PyPT** emits blue fluorescence with the maximum emission peak at 461 nm in THF (10^{-5} M) solution under irradiation (λ_{ex} = 383 nm). Using λ_{ex} = 340 nm as an excitation wavelength, **PyPT** shows a broadened emission band in the range of 365–650 nm, with a dominant emission peak at 460 nm and additional emission peaks at 394 and 560 nm (Figure 2B).

To gain insight into the emission behavior of **PyPT**, concentration-dependent emission spectra were investigated (Figure S6, Supporting information). **PyPT** exhibits a broad emission band with a dominant emission peak at 381 nm and a shoulder peak at 464 nm in ≈10^{-7} M under λ_{ex} = 340 nm irradiation. As the concentration increased to ≈10^{-6} M, a broad emission band was observed with maximum emission peaks at 381 and 461 nm, accompanied by a shoulder emission peak at 570 nm. As the concentration increased from 10^{-6} to 10^{-3} M, the short-wavelength emission peak at 381 nm gradually disappeared, and the emission peak at 462 nm became a dominant peak with a slight redshift (ca. 80 nm). Under λ_{ex} = 383 nm irradiation, **PyPT** also emits dual emissions with peaks at 420 and 470 nm. The maximum emission peak at 461 nm gradually became dominant as the concentration increased from 10^{-7} to 10^{-3} M. The time-resolved fluorescence spectroscopy of compound **PyPT** was measured. Under irradiation at λ_{ex} = 340 nm, the fluorescence lifetimes (τ) of each emission peak are 7.8 ns at 390 nm, 6.21 ns at 460 nm, and 4.89 ns at 570 nm. When irradiated at λ_{ex} = 383 nm, the emission peak at 461 nm shows a lifetime of 6.28 ns (Figure 2C). These results indicate the long-wavelength emission at 570 nm may originate from excimer emission under higher energy excitation, while the emissions at λ_{em} = 460 or 461 nm arise from a similar energy level via a radiative decay channel. Additionally, the yellow solid compound PyPT exhibits a maximum emission band at 465 nm with a fluorescence lifetime of 5.06 ns in the solid state (Figure 2D,E).

Furthermore, the solvent polarity-dependent emission behavior was also measured. Although the solvent polarity shows a slight effect on the UV–vis absorption spectra, **PyPT** exhibits a differentiated emission behavior at 10^{-5} M in various solvents at different excitation wavelengths. Using λ_{ex} = 340 nm as the excitation wavelength, the emission peak at 370 nm slightly changed, while the emission peaks at 470 and 570 nm were red shifted as the solvent polarity increased from cyclohexane to dimethyl sulfoxide (DMSO) (Figure 2F and Table S1, Supporting information). Under λ_{ex} = 383 nm irradiation, **PyPT** exhibits a resolved emission peak at 431 nm in cyclohexane, which gradually redshifted to 490 nm in DMSO (Figure 2G and Table S1, Supporting information). Thus, **PyPT** exhibits excitation wavelength-dependent emission behavior.

2.3. Piezoelectric Properties of PyPT

Inspired by the inherent piezoelectric characteristics of non-centrosymmetric single crystals, we investigated the piezoelectric properties of **PyPT** by applying a strain using a precise programmable motor. **Figure 3A** illustrates the metal-organic semiconductor-metal (MOM) structure of the piezoelectric device, where the single crystal **PyPT** was fixed on a flexible polyimide (PI) substrate using source-drain silver paste electrodes with a channel width of 28 µm. The strain induced in the crystal **PyPT** is estimated using the equation $\varepsilon = \frac{d \sin\theta}{L}$,[39] where ε is the strain, d is the thickness of the substrate, θ is the angle between the tangent line at the end of the substrate and the horizontal line, and L is the length of the horizontal line from one end of the

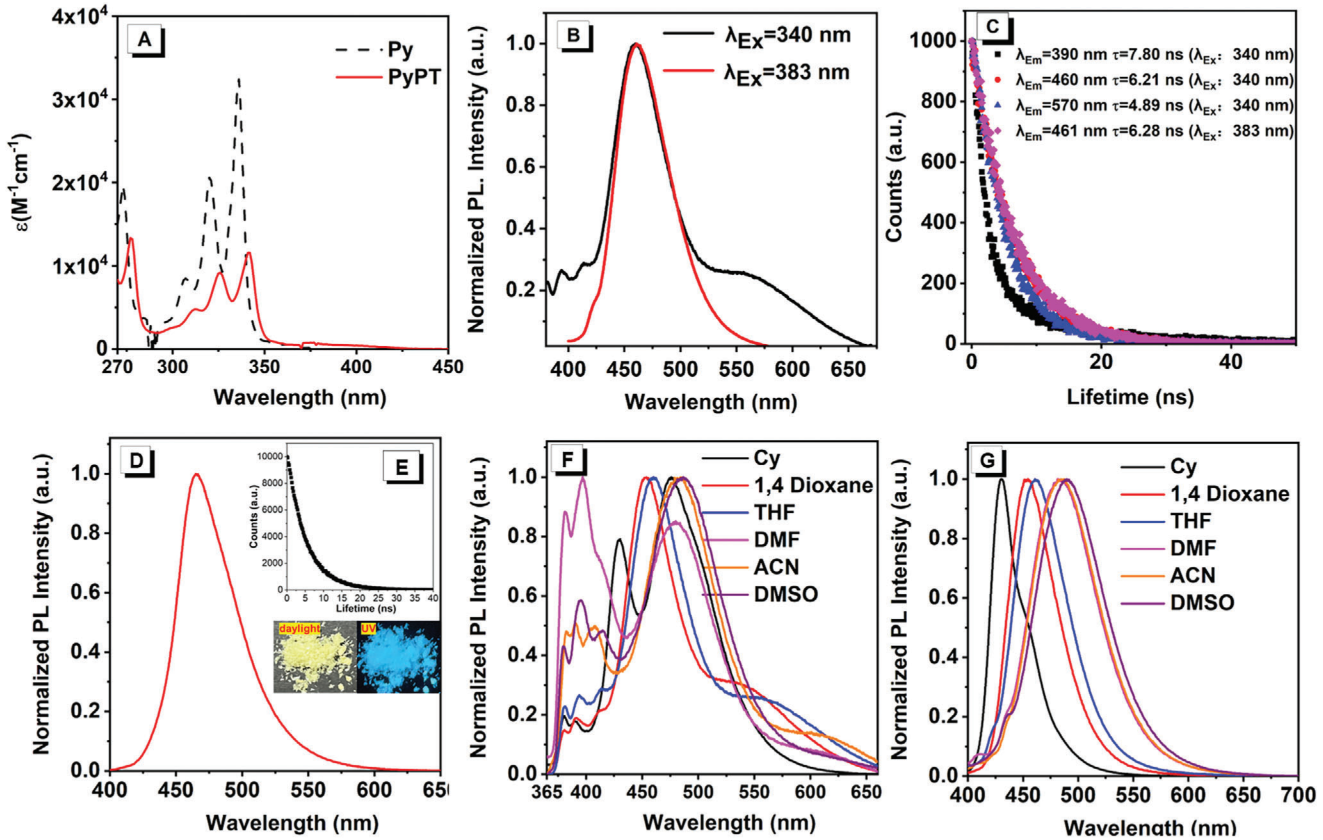

Figure 2. Characterization of the photophysical properties of **PyPT**. A) UV–vis spectra of compounds pyrene (blank) and **PyPT** (red) in THF solution. B) Fluorescence spectra of **PyPT** in THF solution (black: λ_{ex} = 383 nm, red: λ_{ex} = 340 nm). C) Fluorescence decay curves of compound **PyPT** in THF solution under λ_{ex} = 340 nm and λ_{ex} = 383 nm irradiation, respectively. D) Fluorescence spectra of **PyPT** in the solid state. E) Time-resolved fluorescence decay curves of compound **PyPT** in the solid state. Inset: photograph of compound **PyPT** in the solid state under daylight (left) and UV irradiation (right). PL spectra of **PyPT** in different polar solvents at 25 °C F) under λ_{ex} = 340 nm and G) λ_{ex} = 383 nm irradiation.

substrate to the other (Figure 3A). The crystal orientation definition for **PyPT** is presented in Figures S4,S5 (Supporting information).

Both ends of the flexible polyimide film containing the piezoelectric device were fixed to a motor, which induced periodic motion to apply strain along either the (010) or (100) direction. This setup allowed the crystal PyPT-based piezoelectric device to output a stable, periodic, and fast-response piezoelectric signal. As shown in Figure 3B, and Figure S9 (Supporting information), the device outputs a stable current output of 30 pA with an external strain as low as 0.12%. As the strain increased from 0.12% to 0.59%, the maximum current output reached 721 pA. Furthermore, the piezoelectric signal of **PyPT** exhibits significant crystal orientation dependence, being more sensitive in the (010) direction compared to the (100) direction, and the disparity of piezoelectric output current is more pronounced as the tensile strain increased (Figure 3C and Figure S10, Supporting information). This sensitivity difference is attributed to the anisotropy of the strain-induced polarized charges. Moreover, as acceleration increased from 0.3 to 2.7 m s^{-2}, the peak time of the piezoelectric output signal, measured from 0 to the maximum output, gradually shortened from 12 to 9 ns. Beyond this point, the peak time remained constant, even with further increases in acceleration (Figures 3D,E and Figures S13,S14, Supporting information). This characteristic of the PyPT-based piezoelectric device enables it to deliver a stable output signal in high-frequency motion environments, making it suitable for dynamic applications. In addition, it was found that the output did not show a clear change in current before and after polarization by applying a bias polarity of +5 and -5 V to the piezoelectric components, confirming that the bias polarity had no effect on this organic crystal material (Figure S15, Supporting information).

The piezoelectric response of PyPT may be influenced by the thickness of both the PyPT layer and its supporting polyimide substrate. According to flexural rigidity theory, the bending stiffness ($D = E{\cdot}t^3/12(1-\nu^2)$) of each layer impacts strain distribution, which could alter the piezoelectric performance of PyPT. Specifically, a thicker PyPT layer may increase output under strain, while thinner layers may improve sensitivity to small deformations. Given the similarity in Young's modulus between polyimide and PyPT, strain transfer across the interface is likely sensitive to thickness variations. A thinner polyimide substrate might concentrate strain more effectively within the PyPT layer, potentially enhancing the piezoelectric response. Conversely, a thicker substrate could reduce strain transfer, limiting sensitivity (Figures S9–S12, Supporting information). Although our current work focuses on a standard polyimide thickness of 100 µm, future studies will systematically vary PyPT thickness to optimize

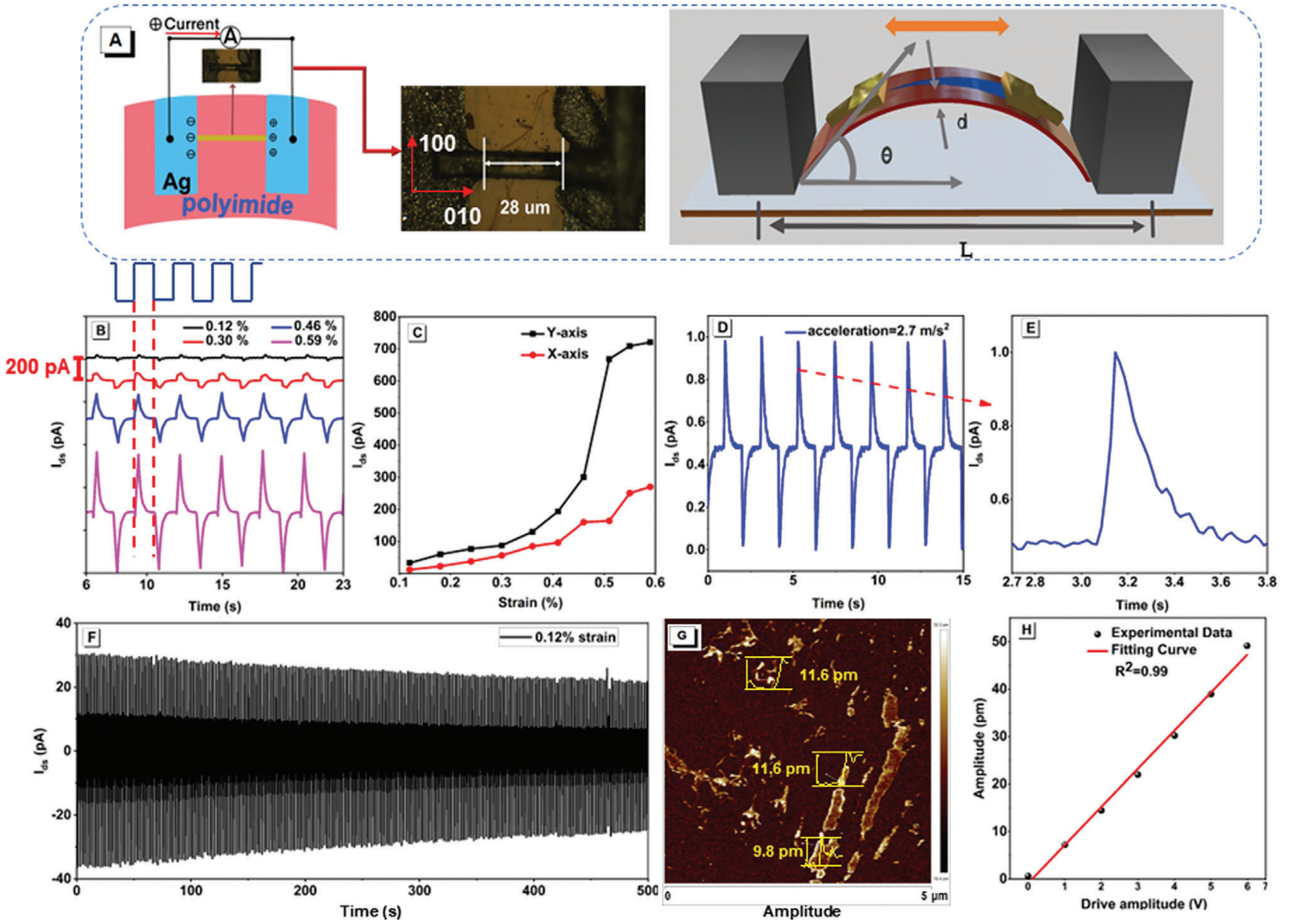

Figure 3. Characterization of the piezoelectric properties of PyPT. A) The schematic diagram and optical microscopy image of the piezoelectric sensor. B) Current outputs of PyPT-based piezoelectric sensors under cyclic strains applied along the (010)-axis (0.12%, 0.30%, 0.46%, 0.59%). C) The relationship between current outputs and applied strains along the Y (010) and X (100) directions. D,E) The response time of the PyPT piezoelectric device at 0.2% strain along the (010)-axis at 2.7 m s-2. F) The mechanical stability of current output of a PyPT piezoelectric device for continuous operation of 500 s under a 0.12% strain. G) Height profile measured with an AFM image. H) Average piezo-response amplitude as a function of applied driving amplitude.

piezoelectric sensitivity and output for specific applications. On the other hand, the piezotronic behavior of the thickness of polyimide film (100 and 250 μm) was measured under the same conditions. As shown in Figure S16A,B, extremely low electrical output was observed from both polyimide films, In addition, as the strain increased from 0.18% to 0.51%, the electrical signal of polyimide film (100 μm) slightly changed (≈20 pA) (Figure S17, Supporting information). The Signal-to-Noise Ratio (SNR) of the PyPT device is calculated as 96, indicating that the PyPT-based piezoelectric device is a great sound detector (Figure S16C, Supporting information).

Furthermore, the crystal PyPT-based piezoelectric device maintained a stable current output of over 22 pA, with only a 22% reduction in maximum output, even after 500 s of continuous operation under 0.12% strain (Figure 3F). This performance is comparable to that of 1D tin dioxide (SnO_2) microwires.[40] Additionally, the piezoelectric properties of the organic crystal PyPT – including piezoelectric signal, piezoelectric coefficient, and Young's Modulus (GPa) – exceed those of previously reported low-dimensional and composite material-based flexible devices (Table S4, Supporting information).

Achieving a rapid response and high stability poses substantial challenges for commercializing flexible piezoelectric materials and devices. Based on the above-mentioned experimental results, this piezoelectric device presents heightened sensitivity and an expansive surface area, unveiling the potential of organic flexible sensors for wearable applications. In this study, we utilized Piezoresponse Force Microscopy (PFM) to evaluate the piezoelectric properties of materials.[41] We measured that Young's modulus of **PyPT** is 1.63 Gpa, lower than most inorganic piezotronics materials and the typical conjugated polycyclic aromatic hydrocarbons-based crystals.[42,43] These results indicated this pure organic molecule is more flexible.[44–46]

One end of the rod-like crystal PyPT was fixed onto a silicon wafer using a silver paste, with the silicon wafer in contact with the conductive sample stage via copper adhesive. When the AFM tip scanned over a 5 μm range on the crystal surface, vertical deformation of 9.8–11.6 pm was observed under an applied 3 V driving voltage Figure 3G,H. The piezoelectric coefficient (d_{33}) was quantified by plotting the piezoelectric amplitude as a function of the driving voltage. The piezoelectric response displacement is linearly related to the driving voltage, and the d_{33} value obtained by linear fitting is about 8.02 ± 0.26 pm V^{-1}, further confirming the intrinsic piezoelectric properties of the single crystal of **PyPT**.

2.4. Flexible Piezotronics Devices for Sound Detection and Recognition

Piezotronics is an emerging field that combines piezoelectric materials with semiconductor technology to create devices that can convert mechanical energy into electrical signals and vice versa, with the potential to revolutionize how we harness and interact with mechanical energy in electronic systems. Sound detection technology requires promptly recognizing and responding to acoustic changes in the environment, such as unusual noises from industrial equipment or alarms from safety systems, which is crucial for maintaining the safety of equipment operation and environmental monitoring.

Piezoelectric materials can be used to detect and convert sound waves into electrical signals, enabling applications in sound sensors and microphones. Currently, inorganic piezoelectric materials like barium titanate have lower mechanical strength and are prone to fracture under strong vibrations or pressure.[47] More importantly, these materials are difficult to degrade and pose environmental hazards. Therefore, it is essential to explore a new generation of organic materials with low toxicity, rapid response, and good flexibility in the field of sound recognition. Organic piezoelectric materials can offer these benefits, making them ideal candidates for developing advanced sound detection technologies.

To verify the sound recognition ability, the crystal **PyPT**-based piezotronics sensor was attached to a loudspeaker. As shown in **Figure** 4B–E and Figures S18–S20 (Supporting information), when a tapping sound with a steady volume and a frequency of 50 Beats Per Minute (BPM) was applied, the sensor outputs a stable electrical signal of 2 pA. The sound volume and the beat speed were controlled using metronome software (interface shown in Figure S18 (Supporting information), APP by Wuhan Net Power Technology Co., Ltd). A periodic variation in the electrical signal (strong-weak-weak-weak) was observed as the volume changed during the routine. The frequency of the output electrical signal remains steady at 50 BPM. Moreover, as the trapping frequency increased to BPM = 100, the intensity and frequency of the output electrical signal remained unchanged, and the calculated response time is ≈12 ms (Figure S20, Supporting information). These results indicate that the piezotronics sensor can rapidly and sensitively identify sound volume and frequency.

Further, to identify the sensitivity of the sound sensor to different timbres, musical instruments (such as woodblock, electronic organ, and drum) were selected as the acoustic source. As shown in Figure 4C, when maintaining a consistent output volume and frequency (BPM = 100) of the sound, the corresponding frequency of the output electrical signal is consistent with the sound frequency. However, the intensity of the output electrical signal is dependent on the acoustic source from different musical instruments, following the order of drum (2 pA) > electronic organ (1.57 pA) > woodblock (1.14 pA) with an error value of less than 5% (Figure S21, Supporting information). More importantly, under the stimulation of different acoustic sources, the wave shape of the output electrical signal is also different. The differentiation in the fingerprint waveform of the acoustic source offers an efficient way of distinguishing types of musical instruments. Therefore, this crystal **PyPT**-based piezoelectric sensor shows strong potential as a high-performance sound-electronic transducer for applications in sound information storage and acoustic identification.

3. Conclusion

In summary, a new pure organic piezoelectric material, **PyPT**, containing phenothiazine was synthesized via a Pd-catalyzed coupling reaction. The compound exhibits excitation-dependent emission behavior, originating from the variety of terminal substituents on the phenothiazine in the excited state. Moreover, the non-centrosymmetric crystal **PyPT** exhibits a low Young's modulus (1.63 GPa), an anisotropic-dependent piezoelectric property, a large electrical output of 721 pA under a 0.59% strain, and a high d_{33} value of 8.02 ± 0.26 pm V^{-1} along the (010) axis. Furthermore, the crystal **PyPT**-based piezoelectric sensor was demonstrated to be capable of identifying the physical characteristics of sound (such as volume, timbre, etc.) via a visual output electronic signal and the acoustic source from different musical instruments. This research offers a new approach for developing high-performance pure organic pyrene-based molecules with piezoelectric behavior and helps to expand the various potential applications of pyrene-based functional materials and flexible sensors.

4. Experimental Section

Synthesis of PyPT (10-(pyren-1-yl)-10H-Phenothiazine): Under a nitrogen atmosphere, mixture of 1-bromopyrene (**1**) (300 mg, 1.07 mmol, 1.0 eq.), phenothiazine (255.17 mg, 1.28 mmol, 1.2 eq.), CS_2CO_3 (1.7 g, 5.33 mmol, 5 eq.) and t-Bu_3P (1.08 g, 5.34 mmol) in toluene (12 mL) solution was stirred 10 min at room temperature, $Pd(Oac)_2$ (60 mg, 0.27 mmol) were then added, the mixture was stirred and heated to 100 °C for 48 h. After it was cooled, the mixture was quenched by H_2O (50 mL) and extracted by CH_2Cl_2 (50 mL× 3) three times, the combined organic layer was successively washed with water and brine (50 mL) and dried over $MgSO_4$ and evaporated. The residue was purified by column chromatography eluting with hexane to give 10-(pyren-1-yl)-10H-phenothiazine (**PyPT**) (168 mg, 37%). ^1H NMR (400 MHz, $CDCl_3$, δ): 8.38 (s, 1H), 8.28 (s, 2H), 8.18 (d, J = 2.0 Hz, 3H), 8.08 (dd, J = 11.1, 9.8 Hz, 3H), 7.06 (dd, J = 7.6, 1.5 Hz, 2H), 6.77 (d, J = 1.2 Hz, 2H), 6.66 (s, 2H), 5.95 (dd, J = 8.3, 1.1 Hz, 2H). ^{13}C NMR (100 MHz, $CDCl_3$, δ): 131.5, 131.1, 131.0, 129.1, 128.4, 127.1, 127.0, 126.6, 126.6, 126.5, 126.4, 126.4, 125.9, 125.8, 124.8, 122.8, 122.5, 119.7, 116.0. HRMS (FTMS + pAPCI) m/z: $[M + H]^+$ Calcd for $C_{28}H_{18}NS$, 400.1082; Found, 400.1156.

Materials Characterization: ^1H and ^{13}C NMR spectra were recorded on a Bruker AV 400 M spectrometer using chloroform-d solvent and tetramethylsilane as an internal reference. J-values were given in Hz. High-resolution mass spectra (HRMS) were recorded on a LC/MS/MS, which consisted of a HPLC system (Ultimate 3000 RSLC, Thermo Scientific, USA) and a Q Exactive Orbitrap (QE orbitrap type) mass spectrometer. UV–vis absorption spectra and photoluminescence (PL) spectra were recorded on a Shimadzu UV-2600 and the Hitachi F-4700 spectrofluorometer. PL quantum yields were measured using absolute methods using a Hamamatsu C11347-11 Quantaurus-QY Analyzer. The lifetime was recorded on

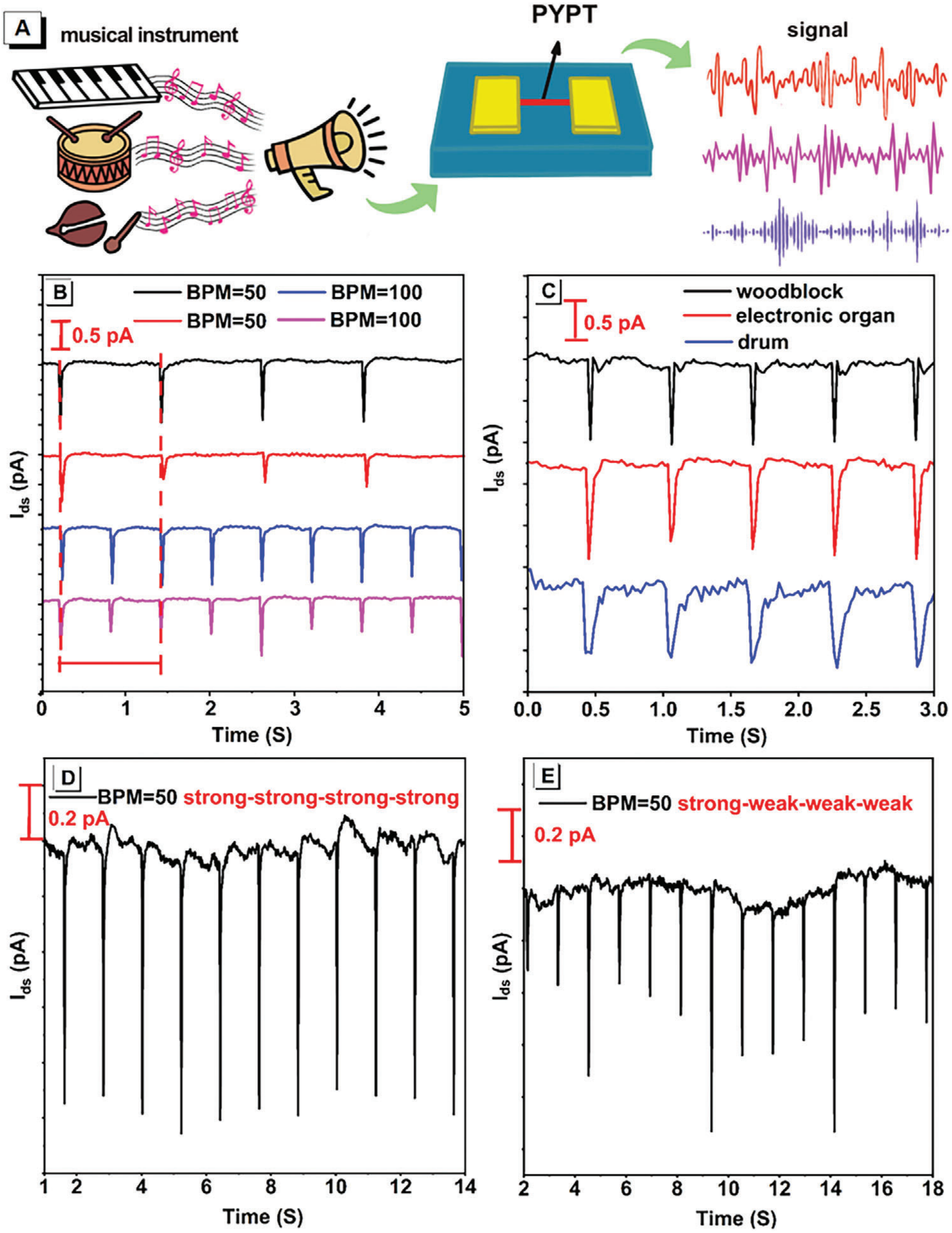

Figure 4. Performance evaluation of the piezoelectric sensor made of PyPT. A) Schematic diagram of the current output of PyPT devices under different conditions. B) Current signals at different volume and frequency sounds. C) Current signals at the same frequency, same size, but different timbres of sound. D) Current output of PyPT devices under fixed frequency (BPM = 50), steady volume. E) Current output of PyPT devices under fixed frequency (BPM = 50) and periodic variation in volume.

an Edinburgh FLS 980 instrument and measured using a time-correlated single-photon counting method. Thermogravimetric analysis was carried on a Mettler Toledo TGA/DSC3+ under dry nitrogen at a heating rate of 10 °C min^{-1}. The quantum chemistry calculation was performed on the Gaussian 09 (B3LYP/6–311G (d, p) basis set) software package.

X-ray Crystallography: Crystallographic data for the compounds was collected on a Bruker APEX 2 CCD diffractometer with graphite monochromated Mo $K\alpha$ radiation ($\lambda = 0.71073$ Å) in the ω scan mode.[48,49] The structures were solved by charge flipping or direct methods algorithms and refined by full-matrix least-squares methods on F,[49,50] All esds (except the esd in the dihedral angle between two *l.s.* planes) were estimated using the full covariance matrix. The cell esds were considered individually in the estimation of esds in distances, angles and torsion angles. Correlations between esds in cell parameters were only used when they were defined by crystal symmetry. An approximate (isotropic) treatment of cell esds was used for estimating esds involving *l.s.* planes. The final cell constants were determined through global refinement of the xyz centroids of the reflections harvested from the entire data set. Structure solution and refinements were carried out using the SHELXTL-PLUS software package.[50] The partially occupied water molecule of crystallization was modeled by the Platon Squeeze procedure. Data (excluding structure factors) on the structures reported here have been deposited with the Cambridge Crystallographic Data Centre. CCDC 2328888 contains the supplementary crystallographic data for this paper. These data could be obtained free of charge from The Cambridge Crystallographic Data Centre via www.ccdc.cam.ac.uk/data_request/cif.

Fabrication of Devices: A rectangular crystal PyPT (dimensions: 180–240 µm in length, 25–31 µm in width, and 16–22 µm in thickness) was placed on a flexible polyimide film (3 cm length × 1 cm width × 100 µm thickness). Both ends of the crystal were fixed using silver paste, serving as electrodes. The fabricated piezoelectric device was tested in ambient air without encapsulation. Over 10 devices were prepared, finding that the electrical signal remained consistent across different crystal dimensions. However, a longer channel length may reduce the device's lifecycle. All devices demonstrated nearly identical electrical responses under the same measurement conditions.

Piezoresponse Force Microscopy (PFM) Measurement: One end of the crystal PyPT was affixed to a silicon wafer with silver paste under microscopic observation. The silicon wafer, containing PyPT crystals, was then positioned on the Atomic Force Microscope (AFM, Bruker, Dimension Fastscan) sample stage, with conductive copper adhesive connecting the sample stage to the silicon wafer. In PFM mode, the AFM was set to a 3 V driving voltage, and the AFM tip scanned a 5 µm range on the crystal surface. The sample's response in both the vertical and horizontal directions was recorded using the AFM's lock-in amplifier to detect surface topography.

Preparation of Crystal PyPT-Based Sound Sensor: A suitable crystal PyPT-based piezoelectric device was selected and attached to the loudspeaker surface with double-sided tape. When sound was played, the device underwent varying degrees of deformation, generating an electrical signal corresponding to the sound volume and beat speed. The sound settings were controlled via software (developed by Wuhan Net Power Technology Co., Ltd.), with an interface shown in Figure S16 (Supporting information). The software allows for four sound volume levels (from weak to strong, levels 1–4) and BPM adjustments from 20 to 200 beats per minute.

Supporting Information

Supporting Information is available from the Wiley Online Library or from the author.

Acknowledgements

X.S., X.W., and W.L. contributed equally to this work. This work was partially supported by the National Natural Science Foundation of China (21975054), and Guangdong Basic and Applied Basic Research Foundation (2020A1515110992). M.S.I. and C.C. acknowledge the financial support from Case Western Reserve University. X.F. thanks Dr. Kai Yan and Ms. Yu Chen (Analysis and Test Center, Guangdong University of Technology) for structure characterization. C.R. thanks the University of Hull for funding support.

Conflict of Interest

The authors declare no conflict of interest.

Data Availability Statement

The data that support the findings of this study are available in the supplementary material of this article.

Keywords

excitation wavelength-dependent emission, flexible sensors, organic piezoelectric materials, organic small molecules, pyrene, wearable electronics

Received: December 12, 2024
Published online:

[1] M. B. Starr, X. Wang, *Nano Energy* **2015**, *14*, 296.
[2] A. M. Manjón-Sanz, M. R. Dolgos, *Chem. Mater.* **2018**, *30*, 8718.
[3] D. P. Dubal, N. R. Chodankar, D. H. Kim, P. Gomez-Romero, *Chem. Soc. Rev.* **2018**, *47*, 2065.
[4] S. Scheffler, P. Poulin, *ACS Appl. Mater. Interfaces.* **2022**, *14*, 16961.
[5] T. Vijayakanth, S. Shankar, G. Finkelstein-Zuta, S. Rencus-Lazar, S. Gilead, E. Gazit, *Chem. Soc. Rev.* **2023**, *52*, 6191.
[6] S. Katzir, *Boston Studies in the Philosophy and History of Science* **2006**, *246*, 273.
[7] B. Stadlober, M. Zirkl, M. Irimia-Vladu, *Chem. Soc. Rev.* **2019**, *48*, 1787.
[8] J. Erhart, *Phys. Educ.* **2013**, *48*, 438.
[9] W. J. Merz, *Nature* **1972**, *236*, 245.
[10] M. Acosta, N. Novak, V. Rojas, S. Patel, R. Vaish, J. Koruza, G. A. Rossetti, J. Rödel, *Phys. Rev. Appl.* **2017**, *4*, 041305.
[11] Y. Zhang, M. Xie, V. Adamaki, H. Khanbareh, C. R. Bowen, *Chem. Soc. Rev.* **2017**, *46*, 7757.
[12] W. R. McCall, K. Kim, C. Heath, G. La Pierre, D. J. Sirbuly, *ACS Appl. Mater. Interfaces.* **2014**, *6*, 19504.
[13] A. Jain, P. K. J., A. K. Sharma, A. Jain, R. P. N., *Polym. Eng. Sci.* **2015**, *55*, 1589.
[14] R. Wang, J. Sui, X. Wang, *ACS Nano* **2022**, *16*, 17708.
[15] Y. Huang, L. Zhang, R. Jing, M. Tang, D. Alikin, V. Shur, X. Wei, L. Jin, *Chem. Eng. J.* **2023**, *477*, 147192.
[16] S. Hurtley, B. Grocholski, *Science* **2019**, *363*, 1297.
[17] P. K. J. Panda, *Mater. Sci.* **2009**, *44*, 5049.
[18] M. Weiss, J. Haufe, M. Carus, M. Brandão, S. Bringezu, B. Hermann, M. K. Patel, *J. Ind. Ecol.* **2012**, *16*, S169.
[19] W. Gao, L. Chang, H. Ma, L. You, J. Yin, J. Liu, Z. Liu, J. Wang, G. Yuan, *NPG Asia Mater* **2015**, *7*, e189.
[20] Z. Zhang, X. Li, Z. Peng, X. Yan, S. Liu, Y. Hong, Y. Shan, X. Xu, L. Jin, B. Liu, X. Zhang, Y. Chai, S. Zhang, A. K. Jen, Z. Yang, *Nat. Commun.* **2023**, *14*, 4094.
[21] L. Li, J. Zhang, C. Yang, L. Huang, J. Zhang, J. Bai, C. Redshaw, X. Feng, C. Cao, N. Huo, J. Li, B. Z. Tang, *Small* **2021**, *17*, 2103125.
[22] S. Sahoo, T. Vijayakanth, P. Kothavade, P. Dixit, J. K. Zareba, K. Shanmuganathan, R. Boomishankar, *ACS Mater. Au.* **2022**, *2*, 124.
[23] Y. M. You, W. Q. Liao, D. Zhao, H. Y. Ye, Y. Zhang, Q. Zhou, X. Niu, J. Wang, P. F. Li, D. W. Fu, Z. Wang, S. Gao, K. Yang, J. M. Liu, J. Li, Y. Yan, R. G. Xiong, *Science* **2017**, *357*, 306.
[24] W. Q. Liao, D. Zhao, Y. Y. Tang, Y. Zhang, P. F. Li, P. P. Shi, X. G. Chen, Y. M. You, R. G. Xiong, *Science* **2019**, *363*, 1206.
[25] F. Mokhtari, B. Azimi, M. Salehi, S. Hashemikia, S. Danti, *J. Mech. Behav. Biomed. Mater.* **2021**, *122*, 104669.
[26] J. Yu, X. Hou, J. He, M. Cui, C. Wang, W. Geng, J. Mu, B. Han, X. Chou, *Nano Energy* **2020**, *69*, 104437.
[27] Y. Huang, G. Rui, Q. Li, E. Allahyarov, R. Li, M. Fukuto, G. J. Zhong, J. Z. Xu, Z. M. Li, P. L. Taylor, L. Zhu, *Nat. Commun.* **2021**, *12*, 675.
[28] X. Feng, X. Wang, C. Redshaw, B. Z. Tang, *Chem. Soc. Rev.* **2023**, *52*, 6715.
[29] T. M. Figueira-Duarte, K. Mullen, *Chem. Rev.* **2011**, *111*, 7260.
[30] A. G. Crawford, A. D. Dwyer, Z. Liu, A. Steffen, A. Beeby, L. O. Palsson, D. J. Tozer, T. B. Marder, *J. Am. Chem. Soc.* **2011**, *133*, 13349.
[31] X. Wang, C. Zhang, J. Zeng, X. Mao, C. Redshaw, G. Niu, X. Yu, X. Feng, *J. Org. Chem.* **2022**, *87*, 12741.
[32] X. Wang, J. Zhang, X. Mao, Y. Liu, R. Li, J. Bai, J. Zhang, C. Redshaw, X. Feng, B. Z. Tang, *J. Org. Chem.* **2022**, *87*, 8503.
[33] J. Ren, Y. Wang, Y. Tian, Z. Liu, X. Xiao, J. Yang, M. Fang, Z. Li, *Angew. Chem., Int. Ed.* **2021**, *60*, 12335.
[34] M. Gao, Y. Tian, X. Li, Y. Gong, M. Fang, J. Yang, Z. Li, *Angew. Chem., Int. Ed.* **2023**, *62*, 202214908.
[35] J. Wang, Z. Chai, J. Wang, C. Wang, M. Han, Q. Liao, A. Huang, P. Lin, C. Li, Q. Li, Z. Li, *Angew. Chem., Int. Ed.* **2019**, *58*, 17297.
[36] Y. Deng, W. Yuan, Z. Jia, G. Liu, *J. Phys. Chem. B.* **2014**, *118*, 14536.

[37] H. Y. Zhang, X. G. Chen, Y. Y. Tang, W. Q. Liao, F. F. Di, X. Mu, H. Peng, R. G. Xiong, *Chem. Soc. Rev.* **2021**, *50*, 8248.

[38] M. Shehzad, S. Wang, Y. Wang, *Npj Flex. Electron.* **2021**, *5*, 237458905.

[39] J.-N. Kim, J. Lee, T. W. Go, A. Rajabi-Abhari, M. Mahato, J. Y. Park, H. Lee, I.-K. Oh, *Nano Energy* **2020**, *75*, 104904.

[40] L. Li, W. Gao, H. Chen, K. Zhao, P. Wen, Y. Yang, X. Wang, Z. Wei, N. Huo, J. Li, *Adv. Electron.* **2020**, *6*, 1901441.

[41] H. Y. Zhang, X. G. Chen, Y. Y. Tang, W. Q. Liao, F. F. Di, X. Mu, H. Peng, R. G. Xiong, *Chem. Soc. Rev.* **2021**, *50*, 8248.

[42] K. Yang, X. Xu, B. Yang, B. Cook, H. Ramos, N. M. A. Krishnan, M. M. Smedskjaer, C. Hoover, M. Bauchy, *Sci. Rep.* **2019**, *9*, 8739.

[43] Z. Han, Y. Cui, Q. Meng, M. He, X. Yan, *Chem. Phys. Lett.* **2021**, *781*, 138982.

[44] G. Simmons, H. Wang, *MIT Press* **1971**, 133.

[45] J. Zeng, T. Liang, J. Zhang, D. Liu, S. Li, X. Lu, M. Han, Y. Yao, J. B. Xu, R. Sun, L. Li, *Small* **2024**, *20*, 2309338.

[46] R. Wu, L. Yan, Y. Zhang, J. Ren, D. Bao, H. Zhang, Y. Wang, S. Du, Q. Huan, H.-J. Gao, *J. Phys. Chem. C* **2015**, *119*, 8208.

[47] M. Shehzad, S. Wang, Y. Wang, *npj Flex. Electron.* **2021**, *5*, 24.

[48] Bruker APEX2 (Version 2.2012.2 0) and SAINT (Version 7.68A), Bruker AXS Inc., Madison, Wisconsin, USA, **2009**.

[49] *SHELXTL V5. 1 software reference manual. GM Sheldrick* -, Bruker AXS Inc., Madison, Wisconsin, USA, **1997**.

[50] G. M. Sheldrick, SHELXS97 and SHELXL97: Program for Crystal Structure Solution and Refinement, University of Göttingen, Germany, **1997**.